An Unusual Mid-infrared Flare in a Type 2 AGN: An Obscured Turning-on AGN or Tidal Disruption Event?

Qian Yang[1], Yue Shen[1,2,7] , Xin Liu[1,2] , Xue-Bing Wu[3,4] , Linhua Jiang[4] , Jinyi Shangguan[5], Matthew J. Graham[6] , and Su Yao[4]

[1] Department of Astronomy, University of Illinois at Urbana-Champaign, Urbana, IL 61801, USA; qiany@illinois.edu
[2] National Center for Supercomputing Applications, University of Illinois at Urbana-Champaign, Urbana, IL 61801, USA
[3] Department of Astronomy, School of Physics, Peking University, Beijing 100871, People's Republic of China
[4] Kavli Institute for Astronomy and Astrophysics, Peking University, Beijing 100871, People's Republic of China
[5] Max-Planck-Institut für extraterrestrische Physik, Gießenbachstr. 1, D-85748 Garching, Germany
[6] California Institute of Technology, 1200 E. California Boulevard, Pasadena, CA 91125, USA

Abstract

We report the discovery of an exceptional MIR flare in a Type 2 AGN, SDSS J165726.81+234528.1, at $z = 0.059$. This object brightened by 3 mag in the *Wide-field Infrared Survey Explorer* (*WISE*) $W1$ and $W2$ bands between 2015 and 2017 (and has been fading since 2018), without significant changes ($\lesssim 0.2$ mag) in the optical over the same period of time. Based on the *WISE* light curves and near-IR imaging, the flare is more significant at longer wavelengths, suggesting an origin of hot dust emission. The estimated black hole mass ($\sim 10^{6.5} M_\odot$) from different methods places its peak bolometric luminosity around the Eddington limit. The high luminosity of the MIR flare and its multiyear timescale suggest that it most likely originated from reprocessed dust radiation in an extended torus surrounding the AGN, instead of from stellar explosions. The MIR color variability is consistent with known changing-look AGN and tidal disruption events (TDEs), but inconsistent with normal supernovae. We suggest that it is a turning-on Type 2 AGN or TDE, where the optical variability is obscured by the dust torus during the transition. This MIR flare event reveals a population of dramatic nuclear transients that are missed in the optical.

Unified Astronomy Thesaurus concepts: Active galactic nuclei (16); Accretion (14); Tidal disruption (1696)

1. Introduction

Modern multiepoch and multiwavelength data have enabled a broad range of time-domain studies from stellar transients to persistent variability from AGN. The multiepoch *Wide-field Infrared Survey Explorer* (*WISE*; Wright et al. 2010) data in mid-infrared $W1$ (3.4 μm) and $W2$ (4.6 μm) bands, in particular, can probe the changes in the continuum emission of warm (~ 300 K) or hot (>800 K) dust in different environments. Mid-infrared (MIR) variability has been seen following optical transient/variability events, such as changing-look AGN (CL AGN; Sheng et al. 2017; Ross et al. 2018; Stern et al. 2018; Yang et al. 2018), tidal disruption events (TDE; Blanchard et al. 2017; Jiang et al. 2017), and supernova (SNe) explosion. In these cases, the MIR emission is predominantly thermal radiation from heated dust grains in the dust torus in AGN or from interstellar medium (ISM)/circumstellar medium (CSM) in SNe. In rare cases, nonthermal radiation from relativistic electrons accelerated by the shock waves in supernova remnants (Dwek et al. 1987) or by jet launched in radio-loud AGN (Urry & Padovani 1995) could also make contributions to the observed MIR emission.

The different classes of transients that produce both optical and MIR variability have characteristic spectral features. CL AGN are objects with emerging or disappearing broad emission lines accompanied by large-amplitude continuum variability, possibly caused by changes in the accretion of gas onto the central supermassive black hole (SMBH; LaMassa et al. 2015; MacLeod et al. 2016, 2019; Runnoe et al. 2016; Rumbaugh et al. 2018; Yang et al. 2018). TDEs exhibit emission from helium and/or hydrogen, and some of them additionally show transient iron coronal lines

when a star is disrupted by the SMBH (Komossa et al. 2008; van Velzen et al. 2011; Gezari et al. 2012; Wang et al. 2012; Arcavi et al. 2014; Holoien et al. 2014, 2016, 2019; Komossa 2015). SNe show strong UV/optical brightening with or without hydrogen, silicon, and helium lines due to the core-collapse of a massive star or the thermonuclear explosion of a white dwarf accreting matter from a companion (e.g., Filippenko 1997; Hillebrandt & Niemeyer 2000; Heger et al. 2003).

To date, most of these transient events are discovered by their variability from UV/optical or X-ray surveys and classified by follow-up spectroscopic characterization. However, transient events might be hidden within dusty environments and would not be detectable in optical, UV, or soft X-ray. For example, Mattila et al. (2018) reported a dust-enshrouded TDE discovered in the near-IR. The multiepoch imaging from the *WISE* survey enables systematic discoveries of MIR transient/variable events, which can be cross-correlated with optical light curves. For example, Wang et al. (2018) presented a sample of 14 TDE candidates selecting from AllWISE data with slow declining MIR light curves, while no optical flare is detected in these objects. Assef et al. (2018) identified 45 *WISE*-selected AGN candidates that are highly variable in the MIR using the AllWISE catalog; only seven of them show significant optical variability.

Here we present an exceptional MIR flare in J165726.81+234528.1 (hereafter, J1657+2345) from our ongoing systematic study of *WISE* variability for AGN and galaxies. J1657+2345 is spectroscopically identified as a Type 2 AGN at $z = 0.059$ in SDSS (York et al. 2000). Its MIR light curves remained quiescent until the end of 2015, followed by an exceptionally large flare in both $W1$ and $W2$. Among >1.8 million spectroscopic galaxies in the SDSS fourteenth data release (DR14, Abolfathi et al. 2018), J1657+2345 is identified

---
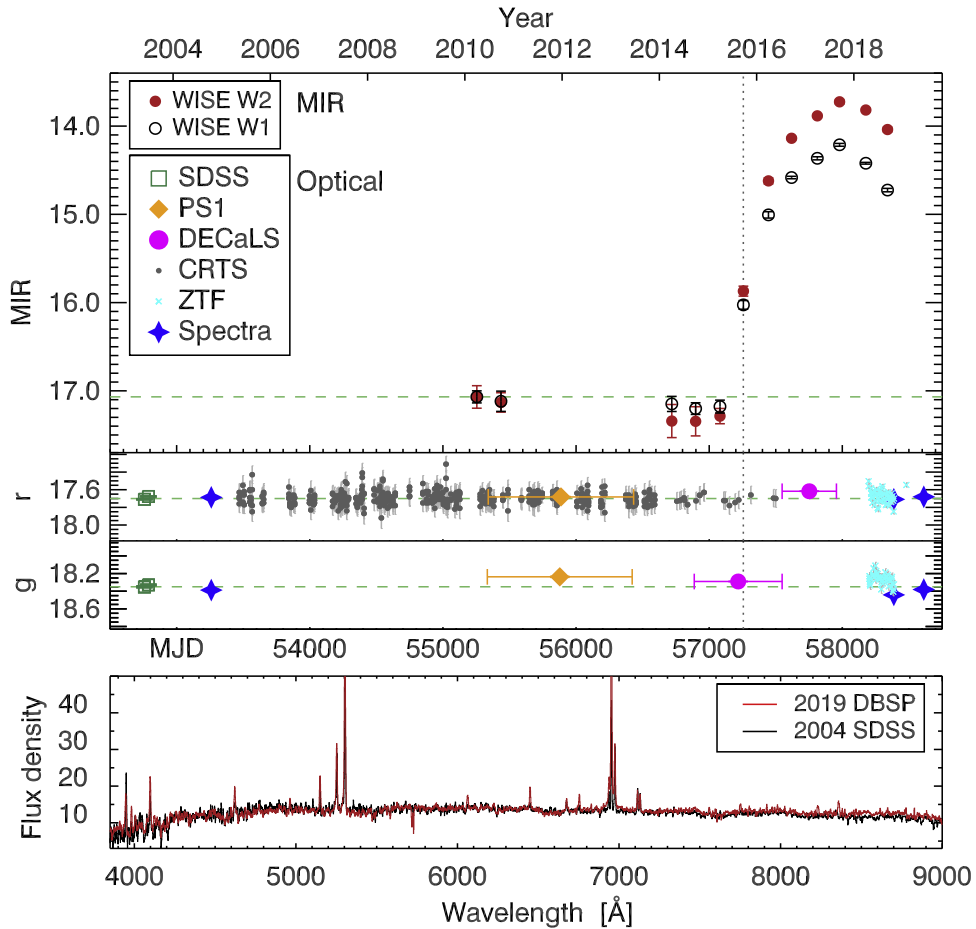
Figure 1. Top panel: light curves of J1657+2345 in MIR from *WISE* and in optical from various surveys, including SDSS, PS1, DECaLS, CRTS, and ZTF. All magnitudes are AB magnitudes. To compare the optical and MIR data, the y-axes in the three panels are plotted on the same scale. The horizontal dashed lines show the earliest epoch magnitude in g, r, and W1 bands from bottom to top panels. The vertical dotted line shows the first *WISE* epoch when the object began to brighten. J1657+2345 flared for more than 3 mag in MIR from 2015 to 2017. However, there is no significant variability in the optical from 2003 to 2019 (constant within 0.2 mag). Bottom panel: Spectra of J1657+2345 taken in 2019 by P200/DBSP (red) and taken in 2004 by SDSS (black). There is no obvious variability between the two optical spectra.

as the most dramatic case with its *WISE* magnitudes brightened by 2.9 and 3.3 mag (a factor of 13.8 and 21.5 increase in flux) in W1 and W2 bands, respectively, between 2015 and 2017. According to the latest *WISE* data taken in 2018 August, J1657 +2345 has passed its peak MIR luminosity and is fading (see Figure 1).

We compiled all available optical photometric data from various surveys, including the SDSS, Pan-STARRS (PS1; Chambers et al. 2016), the Dark Energy Camera Legacy Survey (DECaLS; Dey et al. 2019), the Catalina Real-time Transient Survey (CRTS; Drake et al. 2009), and the Zwicky Transient Facility (ZTF; Bellm et al. 2019). The CRTS data 8 months after the onset of the MIR flare shows that it was still quiescent in the optical. To identify potential spectral variability, we obtained new optical spectra in 2018 September and 2019 May. There is no significant difference between the new spectra and the earlier SDSS spectrum taken in 2004 before the MIR flare. The optical photometric data constrain a maximum variability of ∼0.2 mag before and after the onset of the MIR flare. Thus this object is markedly different from any previous transients first identified in the optical. It is reminiscent of the handful of MIR variable AGN candidates with low optical variability reported in Assef et al. (2018), but

the contrast of the MIR and optical variability is much more extreme. The large difference between the MIR and optical variability motivates a thorough investigation of this event to explore possible scenarios on the nature of the extreme MIR-only flare.

In Section 2, we describe the observations of J1657+2345 in MIR, optical, and near-infrared. We describe the variability, spectral energy distribution (SED), and spectral features of J1657+2345 in Section 3. In Section 4, we compare its MIR variability to CL AGN, TDEs, and SNe. We discuss the timescales of MIR variability from reprocessing the optical/ UV variability with simple geometric dust torus models. We conclude in Section 5. In this paper, we use a ΛCDM cosmology with parameters $\Omega_\Lambda = 0.7$, $\Omega_m = 0.3$, and $H_0 = 70$ km s^{-1} Mpc^{-1}. Unless otherwise specified, all magnitudes are in the AB system (Oke & Gunn 1983).

2. Observations and Data

2.1. WISE *Photometry*

WISE scanned the full sky from 2010 January to July in four bands centered at wavelengths of 3.4, 4.6, 12, and 22 μm (W1, W2, W3, and W4). The secondary cryogen survey and

Table 1
WISE MIR Photometry

Date	MJD	Number	W1	W2	W3	W4
2010 Feb 28	55255	15	17.07 (0.07)	17.07 (0.13)	15.36 (0.16)	14.00 (0.28)
2010 Aug 28	55436	17	17.12 (0.11)	17.13 (0.11)	...	...
2014 Mar 3	56719	14	17.15 (0.09)	17.34 (0.19)	...	...
2014 Aug 29	56898	15	17.20 (0.07)	17.34 (0.17)	...	...
2015 Feb 28	57081	14	17.18 (0.07)	17.29 (0.09)	...	...
2015 Aug 23	57257	17	16.03 (0.05)	15.87 (0.06)	...	...
2016 Feb 27	57445	15	15.01 (0.04)	14.62 (0.03)	...	...
2016 Aug 19	57619	14	14.58 (0.01)	14.14 (0.02)	...	...
2017 Feb 28	57812	17	14.37 (0.02)	13.88 (0.02)	...	...
2017 Aug 14	57979	9	14.21 (0.02)	13.73 (0.03)	...	...
2018 Feb 28	58177	15	14.42 (0.01)	13.82 (0.02)	...	...
2018 Aug 10	58340	9	14.72 (0.02)	14.04 (0.03)	...	...

Note. The *WISE* magnitudes are converted to AB magnitudes. The values in the parentheses are the magnitude errors.

Table 2
Optical Photometry

Survey	Photometry	MJD	Year	g	r	z
SDSS	Model	52788	2003	18.33 (0.01)	17.68 (0.01)	17.05 (0.02)
PS1	Kron	55333–56422	2010–2013	18.24 (0.01)	...	...
		55341–56433	2010–2013	...	17.68 (0.01)	...
		55275–56520	2010–2013	...	...	17.06 (0.01)
DECaLS	Model	56888–57548	2014–2016	18.29 (0.01)	...	...
		57548–57956	2016–2017	...	17.62 (0.01)	...
		57110–57120	2015	...	...	17.02 (0.01)
ZTF	Aperture	58204–58389	2018	18.26 (0.04)	...	...
		58198–58482	2018	...	17.68 (0.03)	...
CRTS	Aperture(unfiltered)	53474–57500	2005–2016	...	17.68 (0.10)	...
SDSS/spec	Spectrophotometry	53260	2004	18.39 (0.01)	17.69 (0.01)	17.12 (0.01)
2.16 m	Spectrophotometry	58387	2018	18.44 (0.01)	17.71 (0.01)	17.26 (0.06)
DBSP	Spectrophotometry	58612	2019	18.38 (0.01)	17.68 (0.01)	17.02 (0.01)

Note. The photometry of PS1 and DECaLS is from stacked images. The magnitudes of ZTF and CRTS in this table are median magnitudes. The compiled light curves show that there is no optical variability (more than 0.2 mag) from 2003 to 2019.

Near-Earth Object Wide-field Infrared Survey Explorer (*NEO-WISE*; Mainzer et al. 2011) Post-Cryogenic Mission mapped the sky from 2010 August to 2011 February. The *NEOWISE* Reactivation Mission (*NEOWISE-R*; Mainzer et al. 2014) surveys the sky in *W1* and *W2* bands from 2013 twice a year. *WISE* obtains ∼10–20 observations within a 36 hr window in each visit. We calculate the median magnitude and magnitude error, specifically the semiamplitude of the range enclosing the 16th and 84th percentiles of all flux measurements within a 6-month window (summarized in Table 1). We limit to good quality single-epoch data points with the best frame image quality score ($qi\_fact = 1$), observed far away from the South Atlantic Anomaly ($saa\_sep \geqslant 5$), with no contamination from the moon ($moon\_masked = 0$), and excluding spurious detection ($cc\_flags = 0$). The *WISE* magnitudes are converted from Vega to AB magnitude as $m_{AB} = m_{Vega} + \Delta m$, where Δm is 2.699, 3.339, 5.174, and 6.620 in *W1*, *W2*, *W3*, and *W4* bands, respectively.

2.2. Optical Photometry

We compile all available optical photometric data from various surveys, including SDSS, PS1, DECaLS, CRTS, and ZTF (see Table 2). J1657+2345 was observed in the SDSS imaging survey in $ugriz_{SDSS}$ bands in 2003 May. As J1657+2345 is an extended source at $z = 0.059$, we use the SDSS model mag, obtained by fitting to de Vaucouleurs (elliptical galaxies) or exponential (spiral galaxies) models to the photometric data. The SDSS gri magnitudes are nearly AB. The SDSS u-band and z-band magnitudes are corrected to the AB system using $u_{AB} = u_{SDSS} - 0.04$ mag and $z_{AB} = z_{SDSS} + 0.02$ mag (Fukugita et al. 1996). J1657+2345 was observed by PS1 (Chambers et al. 2016) from 2010 March to 2014 June in $grizy_{PS1}$ bands. We use the PS1 Kron (1980) magnitude from the PS1 stack catalog. J1657+2345 was observed three times in each band by DECaLS from 2014 August to 2016 June in g_{DECAM} band (3 epochs), from 2016 June to 2017 July in

$r_{\rm DECAM}$ band (3 epochs), and from 2015 March to April in $z_{\rm DECAM}$ band (3 epochs). These images were stacked and presented in the DECaLS DR7 catalog (Dey et al. 2019). We use the DECaLS model magnitude, obtained by fitting five morphological types including point sources, round exponential galaxies with a variable radius, de Vaucouleurs profiles, exponential profiles, or composite profiles. The CRTS (Drake et al. 2009) repeatedly observed a large portion of the sky. J1657+2345 was observed more than 450 times by CRTS from 2005 to 2016. The CRTS data are aperture-based, unfiltered photometry. The ZTF (Bellm et al. 2019) is a new time-domain survey from 2017 in $gri_{\rm ZTF}$ bands. J1657+2345 was covered by ZTF about 50 times in g and r bands from 2018 March to December. The ZTF data are aperture-based photometry with a typical aperture diameter of $2''$.

2.3. Optical Photometric Data Calibration

To calibrate the optical data from different surveys onto the same flux scale, we apply additive corrections to the optical magnitudes taking into account different filter curves and photometry methods. We convert all magnitudes to the AB system. To correct for different filter curves, we convolve the DBSP spectrum (see Section 2.4) with the PS1/DECaLS/ZTF filter curves to obtain synthetic magnitudes, and compare to those derived with the SDSS filters to derive the corrections. Thus the calibration offsets for PS1 are 0.09, 0.02, and -0.06 mag in grz bands; for DECaLS are 0.07, 0.13, and 0.04 mag in grz bands; and for ZTF are 0.06 and 0.13 mag in gr bands. We apply an additional correction for ZTF magnitudes as ZTF uses aperture-based photometry. According to the DECaLS photometry, the offsets between model magnitude and $2''$ aperture magnitude for J1657+2345 are -0.50 and -0.46 mag in g and r bands, respectively. Therefore, ZTF magnitudes are further corrected by -0.44 and -0.33 mag in g and r bands. CRTS data are aperture-based photometry and observed unfiltered, so we apply a constant offset $+0.18$ to the CRTS magnitudes to match the median CRTS magnitude (18.50 mag) to the contemporary calibrated PS1 r-band magnitude (18.68 mag). We summarize the calibrated grz photometry in Table 2.

2.4. Spectroscopic Observations

J1657+2345 was observed by SDSS on 2004 September 12. The SDSS spectroscopy covers a wavelength range from 3820 to 9185 Å with a spectral resolution of $R = \lambda/\Delta\lambda \sim 2000$ (Abazajian et al. 2009) and a spectral binning of 69 km s^{-1} per pixel. The median signal-to-noise ratio (S/N) per pixel of the SDSS spectrum for J1657+2345 is 15. J1657+2345 has no obvious broad emission lines in the spectrum. The narrow emission line flux ratios suggest it is photoionized by AGN, with log([O III/$H\beta$] = 0.65 ± 0.01 and log([N II]/$H\alpha$] = -0.24 ± 0.01 (Kauffmann et al. 2003). Therefore, J1657+2345 is a Type 2 AGN, specifically, a Seyfert 2 galaxy according to the division line between Seyferts and LINERs (Cid Fernandes et al. 2010). The stellar velocity dispersion $\sigma_* = 60.8 \pm 11.2$ km s^{-1}, measured from the SDSS spectrum (Thomas et al. 2013). Using the local relation between SMBH mass $M_{\rm BH}$ and σ_* (Kormendy & Ho 2013), we estimate a BH mass of $10^{6.2\pm0.2}\,M_\odot$. The measured σ_* may be unreliable given SDSS's spectral resolution, therefore we will use different approaches to cross-check the BH mass estimate (Section 3).

We obtained an optical spectrum using the Xinglong 2.16 m telescope in China on 2018 September 26. We use the Beijing Faint Object Spectrograph and Camera (BFOSC) with Grism 4. The object was observed under seeing $\sim 2''$, so we used a slit width of $2''.3$. This instrument configuration yields a dispersion of 198 Å mm^{-1}, a wavelength coverage from 3850 to 8860 Å, and a resolution of $R \sim 265$ (Fan et al. 2016). The object was observed with one exposure of 1800 s. We observed a standard star with the same configuration, HD 161817, for flux calibration. The spectrum was reduced using standard IRAF routines (Tody 1986, 1993). The median S/N per pixel of the 2.16 m spectrum is 6.

We obtained another optical spectrum using the Palomar P200/DBSP spectrograph on 2019 May 9. We used DBSP with the G600 grating on the blue side with a central wavelength of 4000 Å and G316 grating on the red side with a central wavelength of 7500 Å. The object was observed with a $1''.5$ slit under seeing $\sim 1''.2$. This configuration yields a dispersion of 71 Å mm^{-1} and a resolution of $R \sim 969$ at 4000 Å on the blue side; a dispersion of 135 Å mm^{-1} and a resolution of $R \sim 958$ at 7500 Å on the red side. We obtained one exposure of 900 s. We observed a standard star, BD +28d4211, for flux calibration. The DBSP spectrum covers a wide wavelength range, and the median S/N per pixel from 3800 to 9200 Å is 9.

The spectra were taken in smaller aperture/slit than photometry, and J1657+2345 is an extended source. To correct for aperture loss, we calculate spectrophotometry by convolving the spectra with SDSS grz filter curves and compare the spectrophotometry with photometry. We applied a constant scaling factor to the SDSS spectrum, specifically a factor of 1.95, to match the SDSS spectrophotometry in r band to SDSS r-band model photometry. We apply the same scaling factor to other spectra as their [O III] fluxes are consistent with that of the SDSS spectrum (see Section 3.3).

2.5. Near-infrared Photometry

J1657+2345 was observed by the Two Micron All Sky Survey (2MASS; Skrutskie et al. 2006) on 2002 February 12 in J, H, and Ks bands. We downloaded the J, H, and K_s band images from NASA/IPAC Infrared Science Archive (IRSA),[8] and performed aperture photometry on the images using the Python package `photutils`.[9] The source-free background is fitted and subtracted with a two-dimensional third-order polynomial function, which is flexible to fit the large-scale background gradient but robust not to fit the small-scale variation due to the source. The flux of the source is integrated over a circular aperture of $4''$ in radius, and the local background is measured and removed with an annulus of radii between $25''$ and $35''$. By increasing the aperture radius until $12''$, we find that the $4''$ aperture size is large enough to enclose (more than 95% of the total flux). No aperture correction is applied. Our new measurements are systematically brighter than the 2MASS point-source catalog results, by 0.29, 0.32, and 0.45 magnitude, respectively, for J, H, and K_s bands. However, our results are more consistent with the optical spectra and match the stellar emission model better (see Section 3.2). We converted the 2MASS Vega magnitudes to AB magnitude as $m_{\rm AB} = m_{\rm Vega} + \Delta m$, where Δm is 0.89, 1.37,
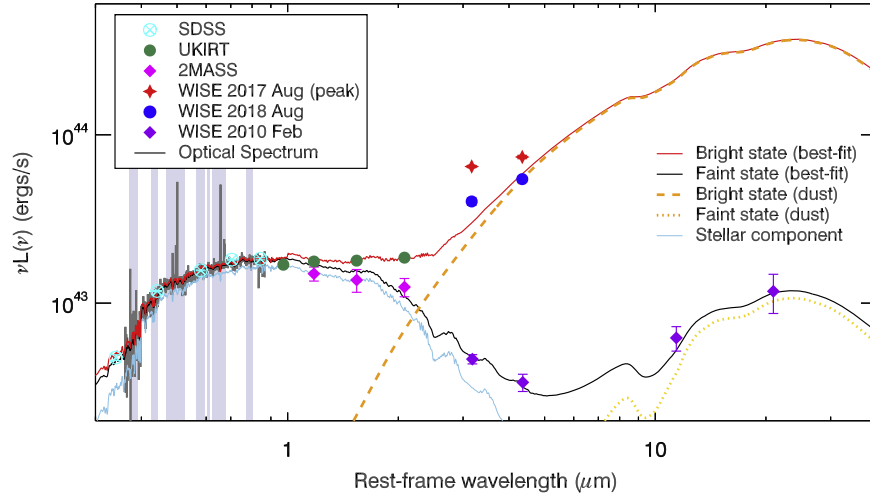
---

[8] irsa.ipac.caltech.edu/
[9] http://photutils.readthedocs.io/

Table 3
Near-infrared Photometry

Instrument	Date	MJD	Y	J	H	K
2MASS	2002 Feb 12	52317	...	16.85 (0.10)	16.68 (0.17)	16.40 (0.13)
UKIRT	2019 Feb 26	58540	16.99 (0.02)	16.72 (0.01)	16.40 (0.01)	16.02 (0.01)

Note. All magnitudes are converted to AB.

Figure 2. SED model of J1657+2345 in the faint state (black) and the bright state (red). We simultaneously fit the spectral and photometric data. The dark gray line is the SDSS spectrum, rescaled to match the SDSS model magnitude (cyan circles with X). The wavelength ranges with strong emission lines are excluded in the fit (shaded regions). We consider stellar emission (light blue solid line), a power-law continuum (negligible), and a clumpy dust radiative transfer model (orange dashed line in bright state, yellow dotted line in faint state). The red stars are *WISE* data in 2017 August, which is the brightest *WISE* epoch. J1657+2345 varies more at redder wavelengths. The hot dust enhanced significantly, while the optical light is not variable.

and 1.84 in J, H, and K_s bands. We summarize the near-infrared photometry of J1657+2345 in Table 3.

We obtained new near-infrared imaging using the United Kingdom Infrared Telescope (UKIRT) on 2019 February 26 in $YJHK$ bands. We used the UKIRT Wide Field Camera (WFCAM) with a four-point dithering pattern in Y band, and eight-point dithering pattern in JHK bands. At each pointing the exposure time was 10 s. WFCAM data were processed by the Cambridge Astronomical Survey Unit. We use UKIRT photometry derived from a $4''$ radius aperture for comparison with the 2MASS photometry. We converted the UKIRT Vega magnitudes to AB magnitude as $m_{\rm AB} = m_{\rm Vega} + \Delta m$, where Δm is 0.634, 0.938, 1.379, and 1.900 in $YJHK$ bands (Hewett et al. 2006).

3. Results

3.1. Variability of J1657+2345

Figure 1 displays the multiwavelength light curves for J1657+2345 from our collected data. From 2010 to 2015, J1657+2345 was scanned by *WISE* five times, during which it remained in the faint state. 2015 August 23 was the first epoch when *WISE* captured the flare. It flared by 1.15 and 1.42 mag in $W1$ and $W2$ bands within half a year from 2015 February to August. It continued to brighten from 2015 to 2017. The peak-luminosity epoch caught by *WISE* is 2017 August 14, with $W1 = 14.21$ and $W2 = 13.73$ (AB magnitude). It brightened by 2.97 and 3.56 (a factor of 13.8 and 21.5 flux increase) in $W1$ and $W2$ bands during 2.5 yr. The *WISE* observation on 2018 February 28 indicates that it started to fade. It was still in the bright state at the latest public *WISE* epoch (2018 August 10), 2.46 and 3.25 mag brighter than its faint state, in $W1$ and $W2$ bands.

However, there is no significant variability in the optical from 2003 to 2019. The optical photometric data from various surveys (summarized in Table 2) are consistent with each other within ~0.2 mag. The continuous CRTS data from 2005 to 2016 is constant with a standard deviation of 0.07 mag. The stacked DECaLS r-band photometry from 2016 June 9 to 2017 July 22 is consistent with the SDSS and PS1 photometry within 0.1 mag. The ZTF data from 2018 March to December is also consistent with the SDSS, PS1, and DECaLS photometry within 0.1 mag. Furthermore, we find no evidence for significant flux variations between the SDSS spectrum, the 2.16 m telescope spectrum, and the DBSP spectrum that were taken ~15 yr apart. There is no continuum flux enhancement in the optical spectra compared to its earlier SDSS spectrum (we discuss the details on spectra in Section 3.3).

3.2. SED Fitting

J1657+2345 brightened by 0.6 mag more in the redder $W2$ band than in $W1$ band, a factor of 1.6 more in flux. It brightened by 0.13, 0.28, and 0.38 mag in J, H, and K bands, respectively, comparing the 2MASS and UKIRT photometry. Therefore we confirmed that the J1657+2345 flare is more prominent at longer IR wavelengths.

We construct SEDs well before (faint state) and after (bright state) the onset of the flare. We simultaneously fit the optical spectrum and IR photometric data for each state. In the faint state, we use the SDSS spectrum (2004 September), 2MASS photometry (2002 February), and *WISE* data (2010 February). In the bright state, we use the DBSP spectrum (2019 May), UKIRT photometry (2019 February), and the latest *WISE* data (2018 August).

Figure 2 shows the SED fitting results in both states. To match the IR photometry with larger apertures, the SDSS spectrum (dark gray line) is scaled by a factor of 1.95 to match the SDSS model mag (as described in Section 2.4). We only use segments of continuum without strong line emission.[10] We perform the SED fitting with a Markov chain Monte Carlo (MCMC) method (Shangguan et al. 2018). We adopt the host galaxy stellar emission model that consists of two simple stellar population models (Bruzual & Charlot 2003) with the Chabrier (2003) initial mass function. The young stellar population has an age less than 300 Myr and the old stellar population has an age of 0.3–15 Gyr. The stellar masses and ages are free parameters in the fitting. We incorporate a power-law component to fit the scattered UV emission from the accretion disk, which is found necessary for Type 2 AGN (Bessiere et al. 2017; Zhao et al. 2019). The amplitude and the slope of the power-law model are free parameters in the fitting. A clumpy dust torus model (Hönig & Kishimoto 2017) is used to mainly fit the MIR data. The model templates are calculated with a Monte Carlo radiative transfer method. Hönig & Kishimoto (2017) provided model templates both with and without a wind component. Since we do not have sufficient MIR coverage to fit the torus component, we chose to use the simpler model without the wind to reduce the number of free parameters. Shangguan & Ho (2019) found that this model is able to reproduce the IR SED of type 2 AGNs. The fitting parameters are the inclination angle, the power-law index of the cloud radial distribution, the number of clouds on the equatorial plane, and the vertical scale height. The degeneracy in the geometric parameters makes it difficult to provide a unique physical interpretation of the best-fit torus model (Zhuang et al. 2018), especially with our limited data coverage. Therefore we only use the successful model fits to estimate the torus luminosity.

The results show that the host galaxy is dominated by the old stellar population, with stellar mass $M_{*,old} = 10^{9.59\pm0.02}\,M_\odot$ and age 1.45 ± 0.04 Gyr (summarized in Table 4). Using the relation between stellar mass and black hole mass of AGN in the nearby universe (Reines & Volonteri 2015), we estimate a black hole mass of $10^{5.97\pm0.30}\,M_\odot$, consistent with our earlier estimation using the $M - \sigma_*$ relation.

Since J1657+2345 is highly obscured in the optical, we use its MIR flux to estimate the bolometric luminosity, L_{bol}, at different epochs. We first estimate the 6 μm luminosity, $\lambda\,L_\lambda(6\,\mu m)$, based on our SED fit. We then adopt $L(2\text{–}10\,keV)/\lambda L_\lambda(6\,\mu m) = 0.234$ (Lutz et al. 2004) and the 2–10 keV bolometric correction $L_{bol}/L(2\text{–}10\,keV) = 20$ (e.g., Elvis et al. 1994). For the faint state, we obtained $\lambda L_\lambda(6\,\mu m) = (3.0 \pm 1.9) \times 10^{42}$ erg s^{-1}, and derived $L_{bol,faint} = (1.4 \pm 0.9) \times 10^{43}$ erg s^{-1}. For the bright state, we got $\lambda L_\lambda(6\,\mu m) = (1.0 \pm 0.1) \times 10^{44}$ erg s^{-1}, and derived $L_{bol,bright} = (4.9 \pm 0.1) \times 10^{44}$ erg s^{-1}. To estimate the peak bolometric luminosity, $L_{bol,peak}$, we fit the SED using the *WISE* data at the peak epoch (2017 August), combined with the DBSP spectrum and UKIRT photometry. We derived $\lambda L_\lambda(6\,\mu m) = (1.6 \pm 0.2) \times 10^{44}$ erg s^{-1} at the peak epoch, thus $L_{bol,peak} = (7.5 \pm 0.1) \times 10^{44}$ erg s^{-1}.

J1657+2345 was not detected by the *ROSAT* All Sky Survey observations (Boller et al. 2016) between 1990 June and 1991 August. Assuming a power-law distribution in X-ray photons with a typical photon index of $\Gamma = 2$, we convert the SED-predicted

Table 4
Physical Properties of J1657+2345

Property	Value	Note
$\log(M_{*,old}\,[M_\odot])$	9.59 ± 0.02	Faint-state SED
$\log(M_{*,young}\,[M_\odot])$	7.72 ± 0.22	Faint-state SED
Age$_{*,old}$ [Gyr]	1.45 ± 0.04	Faint-state SED
Age$_{*,young}$ [Gyr]	0.27 ± 0.05	Faint-state SED
$L_{bol,faint}$ [erg s^{-1}]	$(1.4 \pm 0.9) \times 10^{43}$	Faint-state SED
	$(7.57 \pm 0.01) \times 10^{42}$	SDSS $L_{[O\,III]}$
	$(1.35 \pm 0.01) \times 10^{43}$	DBSP $L_{[O\,III]}$
$L_{bol,bright}$ [erg s^{-1}]	$(4.9 \pm 0.1) \times 10^{44}$	Bright-state SED
$L_{bol,peak}$ [erg s^{-1}]	$(7.5 \pm 0.1) \times 10^{44}$	*WISE* 2017 August
$\log(L_{[O\,III]}\,[erg\,s^{-1}])$	40.45 ± 0.01	SDSS spectrum
	40.66 ± 0.01	DBSP spectrum
$\log(L_{H\alpha,broad}\,[erg\,s^{-1}])$	39.86 ± 0.06	SDSS spectrum
	40.53 ± 0.05	DBSP spectrum
FWHM$_{H\alpha,broad}$[km hr^{-1}]	1610 ± 210	SDSS spectrum
	1664 ± 161	DBSP spectrum
$\log(M_{BH}\,[M_\odot])$	6.22 ± 0.28	SDSS σ_* (Kormendy & Ho 2013)
	5.97 ± 0.30	Stellar mass (Reines & Volonteri 2015)
	6.66 ± 0.15	SDSS Hα scattered light (Greene & Ho 2005)
	7.05 ± 0.10	DBSP Hα scattered light (Greene & Ho 2005)

Note. All uncertainties are statistical errors only.

$L(2\text{–}10\,keV)$ to $L(0.1\text{–}2.4\,keV)$. We derive a flux (0.1–2.4 keV) at the faint state of 9.1×10^{-14} erg s^{-1} cm^{-2}, which is below the *ROSAT* flux limit of a few times 10^{-13} erg s^{-1} cm^{-2}.

3.3. Spectral Properties

To obtain emission line properties, we fit the optical spectra with stellar emission, described in Section 3.2, any residual (or scattered) power-law continuum from the AGN,[11] broad-line emission, and narrow-line emission. Figure 3 shows an example of the spectral fitting to the SDSS and DBSP spectra. We summarize some spectral fitting properties in Table 4. We only show fitting to the SDSS and DBSP spectra, because the resolution and S/N of the spectrum taken by Xinglong 2.16 m telescope are lower and there is no measurable variation between this spectrum and the DBSP spectrum (see Table 2).

The [O III]λ5007 luminosity, $L_{[O\,III]}$, from the SDSS and DBSP spectra are $10^{40.45\pm0.01}$ and $10^{40.66\pm0.01}$ erg s^{-1}, respectively. We have scaled the $L_{[O\,III]}$ obtained from the spectra by a factor of 1.95 to correct for aperture losses (described in Section 2.4). We estimate the bolometric luminosity from $L_{[O\,III]}$ following Trump et al. (2015):

$$\frac{L_{bol}}{10^{40}\,erg\,s^{-1}} = 112\left(\frac{L_{[O\,III]}}{10^{40}\,erg\,s^{-1}}\right)^{1.2}. \quad (1)$$

---

[10] We used the following continuum wavelength windows: 2900–3100, 3500–3700, 3900–4260, 4430–4660, 5240–5650, 5950–6050, 6150–6250, 6800–7700, 8000–9000 Å.

[11] However, this residual AGN continuum component is very weak and cannot be well constrained from the spectral fitting (see discussion at the end of Section 3.3).
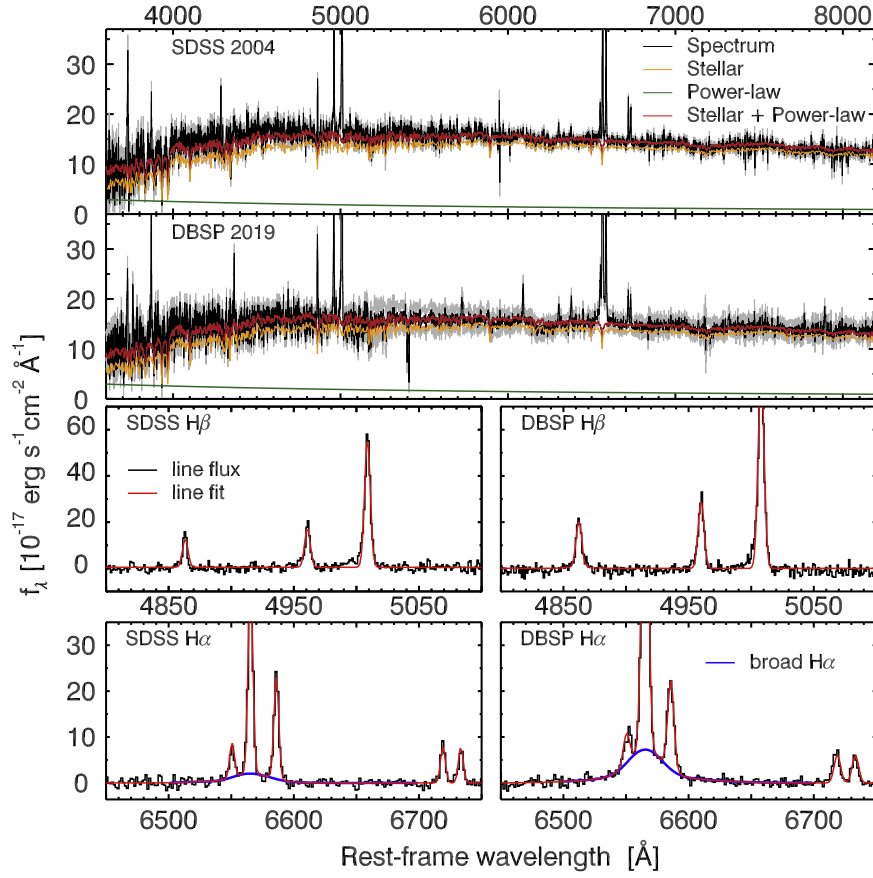
Figure 3. Spectral fits to the SDSS and DBSP spectrum. Top two panels: the data (black), uncertainties (gray), stellar (orange), power-law continuum (green), and total continuum (red). The two spectra are well fitted by the same continuum components. The power-law (AGN) contribution is weak compared to host stellar emission. Bottom four panels: zoom-in for the Hβ and Hα fitting to the SDSS (left) and DBSP (right) spectra. Weak broad Hα is detected in both spectra, which is consistent with scattered broad-line flux in Type 2 AGN (see text). The DBSP spectrum shows stronger broad Hα emission line (blue). No broad Hβ emission is detected in both spectra.

Thus the SDSS and DBSP $L_{\rm [O\ III]}$ corresponds to $L_{\rm bol,faint} = (7.57 \pm 0.01) \times 10^{42}$ and $(1.35 \pm 0.01) \times 10^{43}$ erg s^{-1}, which are both consistent with that obtained from the faint-state SED in Section 3.2. The [O III]λ5007 luminosity in the bright state has not yet responded to the flare, as expected from the $\sim$kiloparsec distances of the narrow-line region gas.

There is weak broad Hα emission detected in both the SDSS and the DBSP spectra. We have tested different fitting recipes for the narrow emission lines and different extraction apertures for the DBSP spectrum and found the broad Hα measurements are robust against these details. The broad-line Hα luminosity, $L_{\rm H\alpha,broad}$, is $10^{39.86 \pm 0.06}$ ($10^{40.53 \pm 0.05}$) erg s^{-1} from the SDSS (DBSP) spectrum, and the FWHM is 1610 ± 210 (1664 ± 161) km s^{-1}. On the other hand, we do not detect broad Hβ emission in the SDSS and DBSP spectra. The expected unobscured broad Hα luminosity, using the measurements for broad-line AGN in Shen et al. (2011), is about 1.5 dex larger than the [O III] luminosity (at $L_{\rm [O\ III]} \sim 10^{40.5}$ erg s^{-1}) in the faint state. Thus we estimate an unobscured broad Hα luminosity of $\sim 10^{42}$ erg s^{-1}. The detected broad Hα flux in the faint state is then roughly 1% of the unobscured broad-line flux. Therefore the detected broad Hα flux is consistent with scattered light in Type 2 AGN (e.g., Zakamska et al. 2005). If this is the case, it is reasonable to see an increase in the broad Hα flux from the faint state to the bright state. The broad Hα flux of the DBSP spectrum (bright state) is a factor of $\sim$5 of

that from the SDSS spectrum (faint state). However, the MIR luminosity increased by a factor of $\sim$20 between the faint and bright states. The UV/optical flare could last much shorter than the MIR flare (see Section 4.2). Therefore the broad Hα flux may have faded significantly when we took the DBSP spectrum.

The width and luminosity of the broad Hα line can be used to estimate the AGN black hole mass (Greene & Ho 2005). Using the detected scattered broad Hα in the SDSS and DBSP spectra, and assuming a scattering fraction of 1% to obtain the unobscured broad Hα luminosity, we estimate a black hole mass of $10^{6.66 \pm 0.15}$ and $10^{7.05 \pm 0.10}$ $M_{\odot}$, which are slightly higher than the black hole masses estimated from stellar mass and σ_*, but broadly consistent given uncertainties in the scattered light fraction and in these BH mass proxies.

The $M_{\rm BH}$ estimates range from $10^{5.97}$ to $10^{7.05}$ using stellar mass, velocity dispersion, and scattered broad Hα flux. We estimate the Eddington ratio $\lambda_{\rm Edd} = L_{\rm bol}/L_{\rm Edd}$, where $L_{\rm Edd} = 1.38 \times 10^{38}(M_{\rm BH}/M_{\odot})$. Using the average value of BH mass ($\sim 10^{6.5}$ $M_{\odot}$) and bolometric luminosity to mitigate uncertainties in individual estimates, we estimate $\lambda_{\rm Edd} \sim 0.02$ for the faint state, $\lambda_{\rm Edd} \sim 1.1$ for the bright state, and $\lambda_{\rm Edd} \sim 1.7$ for the brightest (peak *WISE* flux) state.

The optical continuum is dominated by stellar emission given the Type 2 AGN nature. Using a typical bolometric correction of 10 for AGN continuum luminosity at 5100 Å, λL_{λ}(5100 Å), for unobscured quasars (Shen et al. 2011), and
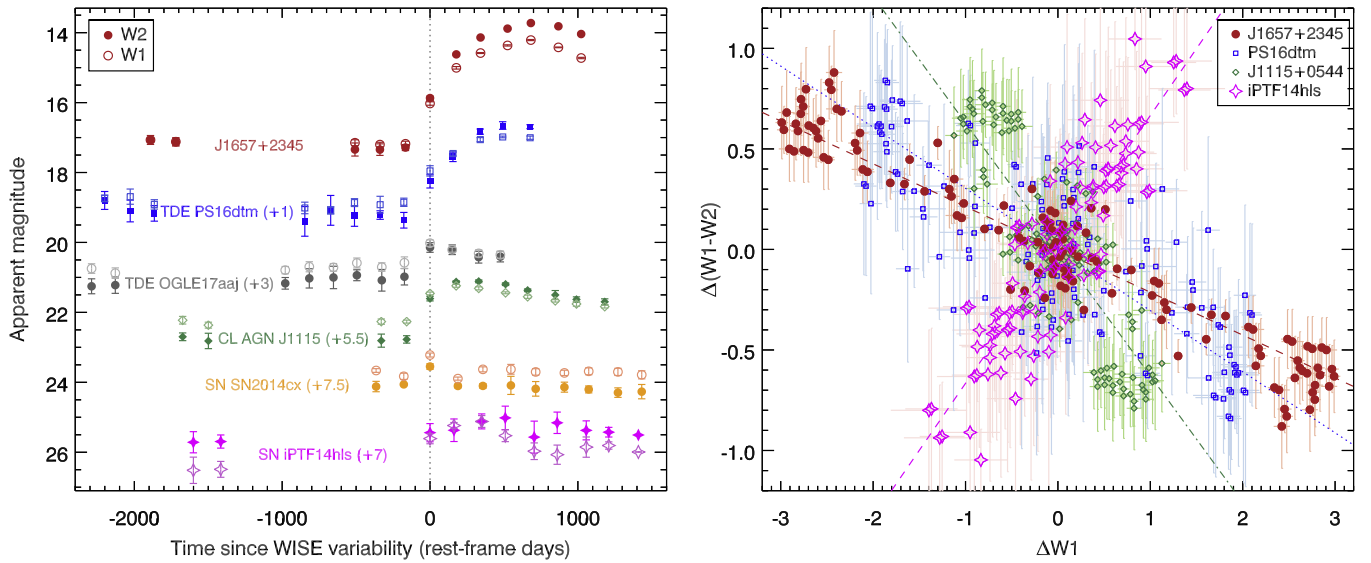
Figure 4. Left panel: MIR light curves of J1657+2345 compared with several known transients. Filled and open shapes represent $W2$ and $W1$ bands, respectively. From top to bottom: J1657+2345 (red), TDE PS16dtm (blue, Blanchard et al. 2017), TDE OGLE17aaj (gray, Gromadzki et al. 2019), CL AGN J1115+0544 (green, Yang et al. 2018), SN SN2014cx (orange, Guillochon et al. 2017), and SN iPTF14hls (magenta, Arcavi et al. 2017). Right panel: MIR color variability, $\Delta(W1 - W2)$, versus magnitude variability, $\Delta W1$, between pairs of epochs from the left panel. J1657+2345 (red filled circles), TDE PS16dtm (blue open squares), and CL AGN J1115+0544 (green open diamonds) are redder-when-brighter due to a stronger hot dust emission in bright states, while SN iPTF14hls (magenta open stars) is bluer-when-brighter, possibly as a result of no hot dust emission.

assuming the same scattering fraction of 1% as for broad Hα, a bolometric luminosity $L_{\rm bol,faint} \simeq 1.4 \times 10^{43}$ erg s^{-1} corresponds to a scattered AGN $\lambda\,L_\lambda(5100\,\text{Å})$ of 1.4×10^{40} erg s^{-1}. This is less than 1% of the total observed continuum at 5100 Å. Thus, even if the obscured optical AGN continuum brightened by a factor of ~20, the observed total flux can only be increased by less than 0.2 mag in r-band, consistent with observations.

4. Discussion

4.1. MIR Variability of Transients

We compare the MIR variability of J1657+2345 with some known transient classes displaying MIR variability, including CL AGN, TDEs, and SNe. We show several examples of light curves in Figure 4. Since J1657+2345 is radio-quiet, the MIR emission is unlikely dominated by jet emission.

Yang et al. (2018) found that many CL AGN exhibit MIR variability. They are redder-when-brighter due to a stronger hot dust contribution in the $W2$ band when the AGN activity becomes stronger.

Some studies (Dou et al. 2016, 2017; Jiang et al. 2016, 2017; van Velzen et al. 2016) reported MIR transient events following a candidate TDE flare in the optical, which were interpreted as signatures of nuclear dust reprocessing the UV/optical flare. We checked the *WISE* MIR light curves of additional TDEs discovered since 2014, when *NEOWISE-R* began continuously scanning the full sky every six months. We found that one TDE OGLE17aaj, discovered by Gromadzki et al. (2019), also displayed an MIR flare. No MIR flare was detected (at >1σ significance) by *WISE* for the other TDEs, including ASASSN-14ae discovered by Holoien et al. (2014), ASASSN-15oi discovered by Holoien et al. (2016), OGLE16aaa discovered by Wyrzykowski et al. (2017), iPTF16axa discovered by Hung et al. (2017), and PS18kh discovered by Holoien et al. (2019).

We study the MIR variability of 2812 SNe discovered from 2014 January to 2018 September from an open catalog for SNe

(Guillochon et al. 2017). $\sim58\%$ of them or their host galaxies were detected by *WISE*. 837 (30%) of them were detected in more than one epoch by *WISE*. Among them, 115 (36) had larger than 0.5 (1) mag variability in $W1$ band. SNe usually brighten in MIR for a shorter timescale (typically caught in one *WISE* epoch, i.e., less than one year) than CL AGN and TDEs (see an example of SN2014cx in the left panel of Figure 4). iPTF14hls is a peculiar SN with long-term (a few years) MIR variability after the explosion, which was classified as type II-P SN and interpreted as a hydrogen-rich explosion of a massive star (Arcavi et al. 2017).

However, the evolution of MIR color of SNe are generally different from those of CL AGN and TDEs. Figure 4 (right) displays the dependence of color variability $\Delta(W1 - W2)$ on the magnitude variability $\Delta W1$ for different populations. We fit a least-squares regression to $\Delta(W1 - W2)$ and $\Delta W1$:

$$\Delta(W1 - W2) = A\Delta W1. \tag{2}$$

We obtain $A = 0.433 \pm 0.005$ for the 837 SNe detected in more than one epoch by *WISE*, and $A = 0.666 \pm 0.045$ for iPTF14hls. On the other hand, we obtain $A = -0.213 \pm 0.018$ for J1657+2345, $A = -0.304 \pm 0.022$ (-0.514 ± 0.042) for TDE PS16dtm (OGLE16aaa), and $A = -0.629 \pm 0.064$ for CL AGN J1115+0544. CL AGN and TDEs (PS16dtm and OGLE16aaa) all display a redder-when-brighter behavior, as a consequence of stronger hot dust radiation from a nuclear dust torus that peaks at wavelengths redder than $W2$ band. SNe, however, display a bluer-when-brighter behavior, possibly caused by the lack of hot dust contribution.

J1657+2345 is redder-when-brighter in MIR, with emerging strong hot dust contribution in the bright state. Thus, we speculate that the J1657+2345 MIR transient is from the dust torus of the central AGN. It is likely that the central black hole of J1657+2345 is increasing its accretion rate as in a CL AGN, or due to a recent TDE embedded in a highly obscuring dust torus. The flare of J1657+2345 is most likely due to TDE or
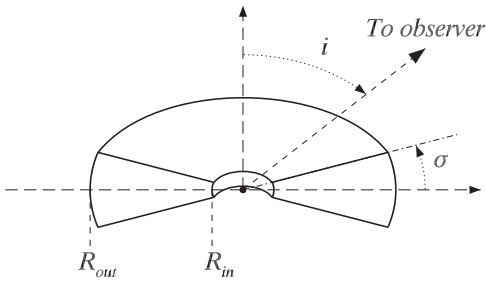
Figure 5. Simple cartoon of the dust torus geometry (e.g., Nenkova et al. 2008). The inner and outer radii are $R_{\rm in}$ and $R_{\rm out}$. σ is the half-opening angle, and i is the inclination angle.

CL AGN events. It is less likely that the MIR flare of J1657 +2345 is due to a normal SN. The explosion of a massive star in the central AGN dust torus still remains a possibility based on the color variability argument. However, the detection of enhanced scattered broad Hα emission and the observed large MIR luminosity of the flare are difficult to explain with stellar explosions.

4.2. Variability Timescales

The MIR flare of J1657+2345 lasts more than three years. The dust torus surrounding the central SMBH responds to continuum variations and reradiates in the infrared. The continuum light arrives at different parts of the reverberating torus region at different times, and the reprocessed light reaches the observer at different later times. Therefore, the extended torus structure can lead to smoothed and stretched MIR light curves than the driving UV/optical light curve.

Here we construct a simple geometrical torus model (illustrated in Figure 5) to demonstrate the geometric effect of the dust torus on the IR echo. In our toy model, the dusty clouds are distributed between inner and outer radii $R_{\rm in}$ and $R_{\rm out}$, with half-opening angle σ and inclination angle i. Following the methodology in Shen (2012), we describe the driving UV/optical continuum flare as a step function at time $t = 0$ followed by a constant flux increment f_c for a period of Δt (see Equation (2) in Shen 2012). We assume a constant density and uniform reprocessing efficiency across the entire torus region.

Figure 6 shows several examples of the responding MIR light curves for a dusty torus with $\sigma = 45°$, $R_{\rm in} = 2$, and $R_{\rm out} = 20$, to a step function UV/optical flare with a duration $\Delta t = 1$. Time is in units of months and distances are in units of light-months. For such a short UV/optical flare, the resulting MIR echo can be extended to ~three years due to the spatial extension of the dust torus. The responding MIR light curves also have different shapes for different inclination angles. The average time delay between the optical/UV flare and the echoed MIR flare is determined by the radial distribution of the reprocessing material but not on inclination angle. The onset of the MIR echo is determined by $R_{\rm in}$, the torus opening angle, and the inclination angle. In our example torus model, the MIR echo should start at most at 2 months after the onset of the optical flare.

The inner radius of the torus is determined by the dust sublimation temperature as (Nenkova et al. 2008)

$$R_{\rm in} \simeq 0.4 \left(\frac{L_{\rm bol}}{10^{45}\,{\rm erg}^{-1}}\right)^{1/2} \left(\frac{1500\,{\rm K}}{T_{\rm sub}}\right)^{2.6}\,{\rm pc}, \qquad (3)$$

where $T_{\rm sub}$ is the dust sublimation temperature and $L_{\rm bol}$ is the bolometric luminosity of the AGN. The innermost dust radius has
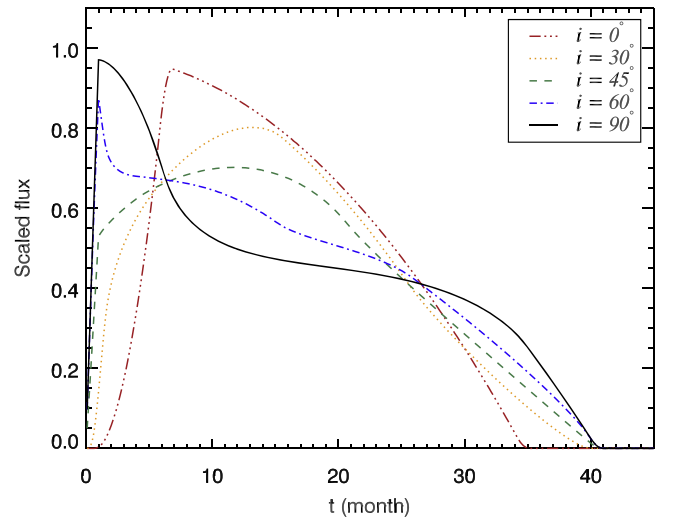
Figure 6. Torus response curves at different inclination angle i of 0° (red, i.e., face-on), 30° (orange), 45° (green), 60° (blue), and 90° (black, i.e., edge-on). The driving UV/optical flare is approximated by a constant flux of f_c between $t = 0$ and $t = 1$ months and zero elsewhere. The responding light curves are much more extended as a consequence of the dust torus extension and the inclination angle.

now been measured by reverberation lags between optical and near-infrared (K-band) for ~20 nearby AGN (e.g., Minezaki et al. 2004; Suganuma et al. 2006; Koshida et al. 2014). The inner dust radii of these AGN range from 10 to 150 light days, and correlate tightly with AGN luminosity, $L_{\rm AGN}$, as $R_{\rm in} \propto L_{\rm AGN}^{0.5}$. It is more difficult to determine the outer boundary of the dust torus. Current observations are consistent with a torus radial thickness $Y = R_{\rm out}/R_{\rm in}$ no more than ~20–30, and perhaps 5–10 (Nenkova et al. 2008). Thus the outer radius is a few light years.

Using the bolometric luminosity $L_{\rm bol,faint} = 1.35 \times 10^{43}$ erg s^{-1} at the faint state, and assuming $T_{\rm sub} = 1500$ K, we obtain $R_{\rm in} \sim 0.05$ pc, corresponding to 55 lt-day. A torus radial thickness $Y = 5$–30 translates to an outer boundary $R_{\rm out}$ of approximately 0.8–4.6 lt-yr. These estimates are similar to the values adopted for our demonstration example described earlier.

J1657+2345 has an estimated BH mass of ~10^6–$10^7\,M_\odot$ (Table 4). For a $M_{\rm BH} = 10^6\,M_\odot$ SMBH, the Schwarzschild radius is $R_S = 2GM_{\rm BH}/c^2 = 3 \times 10^{11}$ cm. The tidal disruption radius is $r_{\rm T} \simeq 5 \times 10^{12} M_6^{1/3}(r_*/r_\odot)(m_*/M_\odot)^{-1/3}$ cm, where $M_6 = M_{\rm BH}/10^6\,M_\odot$, m_* and r_* are the mass and radius of the disrupted star (Rees 1988). Thus the tidal disruption radius of solar-type stars is much larger than the Schwarzschild radius for an $M = 10^6\,M_\odot$ SMBH. The characteristic timescale of TDE, i.e., the orbital period of the most tightly bound debris, is $\Delta t = 0.35 M_7^{1/2}(m_*/M_\odot)^{-1}(r_*/r_\odot)^{3/2} \simeq 0.1$ yr, where $M_7 = M_{\rm BH}/10^7\,M_\odot$ (Lodato & Rossi 2011). Therefore, the observed multiyear MIR light curve for J1657+2345 could be the stretched response to the much shorter TDE UV/optical flare of a few months. Indeed, Mattila et al. (2018) reported a dust-enshrouded TDE in a nearby merging galaxy Arp 299, whose MIR light curves are similar to that of J1657+2345. The low BH mass and the approximately Eddington-limited luminosity near the peak of the light curve makes a TDE a favorable scenario for the flare in J1657+2345.

Rare, rapid CL AGN phenomena have also been observed on timescales of less than 1 yr (Gezari et al. 2017; Yang et al. 2018; Trakhtenbrot et al. 2019a; Yan et al. 2019). Thus the

MIR flare of J1657+2345 could also be the stretched dust echo of such rapid CL AGN events. While in general CL AGN are not TDEs, some of them may be due to TDEs with observed similar decaying light curves. Indeed, the TDE scenario has been invoked to explain specific CL AGN (e.g., Merloni et al. 2015). However, the dramatic changes in the accretion flow onto the SMBH are still not fully understood (e.g., Rumbaugh et al. 2018; Dexter et al. 2019; Trakhtenbrot et al. 2019b), and it is possible that other processes can drive the required UV/optical variability without tidally disrupting a star.

5. Summary

We have discovered an exceptional MIR transient in the Type 2 AGN J1657+2345, with its *WISE* MIR magnitudes brightened by 3 mag from 2015 to 2017. Among more than 1.8 million galaxies in the SDSS DR14, J1657+2345 has the most extreme *WISE* variability amplitude. MIR variability is commonly interpreted as the dust echo of UV/optical variability. However, for this peculiar MIR transient, there is no corresponding optical photometric variability from 2003 to 2019. New optical spectra confirm that there is no significant optical variability, and new near-infrared photometry demonstrates that the MIR flare is more prominent at longer wavelengths. The lack of optical variability distinguishes J1657+2345 from the known population of CL AGN.

We modeled the SEDs and optical spectra of J1657+2345, and estimated a black mass of $\sim 10^6$–$10^7 M_\odot$ and stellar mass of $\sim 10^{9.6} M_\odot$. The bolometric luminosity in the faint state is 1.4×10^{43} erg s^{-1} and in the most recent bright state is 4.9×10^{44} erg s^{-1}. The peak bolometric luminosity is 7.7×10^{44} erg s^{-1}. These estimates place the accretion luminosity of the BH around the Eddington limit in the bright state. Based on energetic grounds and the multiyear long duration of the flare, it would be difficult to associate the MIR flare with stellar explosions and circumstellar dust reprocessing. In addition, the MIR color variability is consistent with CL AGN and TDEs, and inconsistent with normal SNe. We also detected weak broad Hα emission in the faint and bright-state spectra, which is consistent with scattered light from the obscured broad-line region. The enhancement of the scattered broad Hα emission in the latest spectrum also favors the AGN variability and torus reprocessing scenario.

Assuming that the MIR flare comes from the AGN torus reprocessing the UV/optical variability from much closer to the BH, we show that the extended torus geometry can reproduce the multiyear MIR light curve responding to a nuclear UV/optical flare on much shorter timescale of a few months.

Overall our best explanation for the J1657+2345 MIR flare is that it is a rapidly turning-on AGN or TDE that is heavily obscured in the optical in a Type 2 AGN. Such objects are naturally expected as the Type 2 counterparts to the optically unobscured CL AGN population. The discovery of the J1657+2345 flare reveals there is a population of similar nuclear flares that are missed in the optical window. A systematic search of such MIR transients among different types of galaxies will be important to understand nuclear transients in general.

ORCID iDs

Yue Shen ◉ https://orcid.org/0000-0003-1659-7035
Xin Liu ◉ https://orcid.org/0000-0003-0049-5210
Xue-Bing Wu ◉ https://orcid.org/0000-0002-7350-6913
Linhua Jiang ◉ https://orcid.org/0000-0003-4176-6486
Matthew J. Graham ◉ https://orcid.org/0000-0002-3168-0139
Su Yao ◉ https://orcid.org/0000-0002-9728-1552

References

Abazajian, K. N., Adelman-McCarthy, J. K., Agüeros, M. A., et al. 2009, ApJS, 182, 543
Abolfathi, B., Aguado, D. S., Aguilar, G., et al. 2018, ApJS, 235, 42
Arcavi, I., Gal-Yam, A., Sullivan, M., et al. 2014, ApJ, 793, 38
Arcavi, I., Howell, D. A., Kasen, D., et al. 2017, Natur, 551, 210
Assef, R. J., Prieto, J. L., Stern, D., et al. 2018, ApJ, 866, 26
Bellm, E. C., Kulkarni, S. R., Graham, M. J., et al. 2019, PASP, 131, 018002
Bessiere, P. S., Tadhunter, C. N., Ramos Almeida, C., Villar Martín, M., & Cabrera-Lavers, A. 2017, MNRAS, 466, 3887
Blanchard, P. K., Nicholl, M., Berger, E., et al. 2017, ApJ, 843, 106
Boller, T., Freyberg, M. J., Trümper, J., et al. 2016, A&A, 588, A103
Bruzual, G., & Charlot, S. 2003, MNRAS, 344, 1000
Chabrier, G. 2003, PASP, 115, 763
Chambers, K. C., Magnier, E. A., Metcalfe, N., et al. 2016, arXiv:1612.05560
Cid Fernandes, R., Stasińska, G., Schlickmann, M. S., et al. 2010, MNRAS, 403, 1036
Dexter, J., Xin, S., Shen, Y., et al. 2019, arXiv:1906.10138
Dey, A., Schlegel, D. J., Lang, D., et al. 2019, AJ, 157, 168
Dou, L., Wang, T., Yan, L., et al. 2017, ApJL, 841, L8
Dou, L., Wang, T.-g., Jiang, N., et al. 2016, ApJ, 832, 188
Drake, A. J., Djorgovski, S. G., Mahabal, A., et al. 2009, ApJ, 696, 870
Dwek, E., Dinerstein, H. L., Gillett, F. C., Hauser, M. G., & Rice, W. L. 1987, ApJ, 315, 571
Elvis, M., Wilkes, B. J., McDowell, J. C., et al. 1994, ApJS, 95, 1
Fan, Z., Wang, H., Jiang, X., et al. 2016, PASP, 128, 115005
Filippenko, A. V. 1997, ARA&A, 35, 309
Fukugita, M., Ichikawa, T., Gunn, J. E., et al. 1996, AJ, 111, 1748
Gezari, S., Chornock, R., Rest, A., et al. 2012, Natur, 485, 217
Gezari, S., Hung, T., Cenko, S. B., et al. 2017, ApJ, 835, 144
Greene, J. E., & Ho, L. C. 2005, ApJ, 630, 122
Gromadzki, M., Hamanowicz, A., Wyrzykowski, L., et al. 2019, A&A, 622, L2
Guillochon, J., Parrent, J., Kelley, L. Z., & Margutti, R. 2017, ApJ, 835, 64
Heger, A., Fryer, C. L., Woosley, S. E., Langer, N., & Hartmann, D. H. 2003, ApJ, 591, 288
Hewett, P. C., Warren, S. J., Leggett, S. K., & Hodgkin, S. T. 2006, MNRAS, 367, 454
Hillebrandt, W., & Niemeyer, J. C. 2000, ARA&A, 38, 191
Holoien, T. W. S., Huber, M. E., Shappee, B. J., et al. 2019, ApJ, 880, 120
Holoien, T. W. S., Kochanek, C. S., Prieto, J. L., et al. 2016, MNRAS, 463, 3813
Holoien, T. W. S., Prieto, J. L., Bersier, D., et al. 2014, MNRAS, 445, 3263
Hönig, S. F., & Kishimoto, M. 2017, ApJL, 838, L20
Hung, T., Gezari, S., Blagorodnova, N., et al. 2017, ApJ, 842, 29
Jiang, N., Dou, L., Wang, T., et al. 2016, ApJL, 828, L14
Jiang, N., Wang, T., Yan, L., et al. 2017, ApJ, 850, 63
Kauffmann, G., Heckman, T. M., Tremonti, C., et al. 2003, MNRAS, 346, 1055
Komossa, S. 2015, JHEAp, 7, 148
Komossa, S., Zhou, H., Wang, T., et al. 2008, ApJL, 678, L13
Kormendy, J., & Ho, L. C. 2013, ARA&A, 51, 511
Koshida, S., Minezaki, T., Yoshii, Y., et al. 2014, ApJ, 788, 159
LaMassa, S. M., Cales, S., Moran, E. C., et al. 2015, ApJ, 800, 144
Lodato, G., & Rossi, E. M. 2011, MNRAS, 410, 359
Lutz, D., Maiolino, R., Spoon, H. W. W., & Moorwood, A. F. M. 2004, A&A, 418, 465
MacLeod, C. L., Green, P. J., Anderson, S. F., et al. 2019, ApJ, 874, 8
MacLeod, C. L., Ross, N. P., Lawrence, A., et al. 2016, MNRAS, 457, 389
Mainzer, A., Bauer, J., Cutri, R. M., et al. 2014, ApJ, 792, 30
Mainzer, A., Grav, T., Bauer, J., et al. 2011, ApJ, 743, 156
Mattila, S., Pérez-Torres, M., Efstathiou, A., et al. 2018, Sci, 361, 482
Merloni, A., Dwelly, T., Salvato, M., et al. 2015, MNRAS, 452, 69
Minezaki, T., Yoshii, Y., Kobayashi, Y., et al. 2004, ApJL, 600, L35
Nenkova, M., Sirocky, M. M., Nikutta, R., Ivezić, Ž., & Elitzur, M. 2008, ApJ, 685, 160
Oke, J. B., & Gunn, J. E. 1983, ApJ, 266, 713
Rees, M. J. 1988, Natur, 333, 523
Reines, A. E., & Volonteri, M. 2015, ApJ, 813, 82
Ross, N. P., Ford, K. E. S., Graham, M., et al. 2018, MNRAS, 480, 4468
Rumbaugh, N., Shen, Y., Morganson, E., et al. 2018, ApJ, 854, 160
Runnoe, J. C., Cales, S., Ruan, J. J., et al. 2016, MNRAS, 455, 1691
Shangguan, J., & Ho, L. C. 2019, ApJ, 873, 90
Shangguan, J., Ho, L. C., & Xie, Y. 2018, ApJ, 854, 158
Shen, Y. 2012, ApJ, 757, 152
Shen, Y., Richards, G. T., Strauss, M. A., et al. 2011, ApJS, 194, 45
Sheng, Z., Wang, T., Jiang, N., et al. 2017, ApJL, 846, L7
Skrutskie, M. F., Cutri, R. M., Stiening, R., et al. 2006, AJ, 131, 1163
Stern, D., McKernan, B., Graham, M. J., et al. 2018, ApJ, 864, 27
Suganuma, M., Yoshii, Y., Kobayashi, Y., et al. 2006, ApJ, 639, 46
Thomas, D., Steele, O., Maraston, C., et al. 2013, MNRAS, 431, 1383
Tody, D. 1986, Proc. SPIE, 627, 733
Tody, D. 1993, in ASP Conf. Ser. 52, Astronomical Data Analysis Software and Systems II, ed. R. J. Hanisch, R. J. V. Brissenden, & J. Barnes (San Francisco, CA: ASP), 173
Trakhtenbrot, B., Arcavi, I., MacLeod, C. L., et al. 2019a, ApJ, 883, 94
Trakhtenbrot, B., Arcavi, I., Ricci, C., et al. 2019b, NatAs, 3, 242
Trump, J. R., Sun, M., Zeimann, G. R., et al. 2015, ApJ, 811, 26
Urry, C. M., & Padovani, P. 1995, PASP, 107, 803
van Velzen, S., Farrar, G. R., Gezari, S., et al. 2011, ApJ, 741, 73
van Velzen, S., Mendez, A. J., Krolik, J. H., & Gorjian, V. 2016, ApJ, 829, 19
Wang, T., Yan, L., Dou, L., et al. 2018, MNRAS, 477, 2943
Wang, T.-G., Zhou, H.-Y., Komossa, S., et al. 2012, ApJ, 749, 115
Wright, E. L., Eisenhardt, P. R. M., Mainzer, A. K., et al. 2010, AJ, 140, 1868
Yan, L., Wang, T., Jiang, N., et al. 2019, ApJ, 874, 44
Yang, Q., Wu, X.-B., Fan, X., et al. 2018, ApJ, 862, 109
York, D. G., Adelman, J., Anderson, J. E., Jr., et al. 2000, AJ, 120, 1579
Zakamska, N. L., Schmidt, G. D., Smith, P. S., et al. 2005, AJ, 129, 1212
Zhao, D., Ho, L. C., Zhao, Y., Shangguan, J., & Kim, M. 2019, ApJ, 877, 52
Zhuang, M.-Y., Ho, L. C., & Shangguan, J. 2018, ApJ, 862, 118
Wyrzykowski, Ł., Zieliński, M., Kostrzewa-Rutkowska, Z., et al. 2017, MNRAS, 465, L114